Optimizing Thermoacoustic Characterization Experiments for Identifiability Improves both Parameter Estimation Accuracy and Closed-Loop Controller Robustness Guarantees

Xiaoling Chen[a], Jacqueline O'Connor[a]* and Hosam Fathy[b]

[a]*Department of Mechanical Engineering, Pennsylvania State University, University Park, United States;*

 [b]*Department of Mechanical Engineering, University of Maryland, College Park, United States*

* Corresponding author:
Jacqueline O'Connor
111 Research East Building, University Park, PA 16803
814.863.1502, jxo22@psu.edu

Optimizing Thermoacoustic Characterization Experiments for Identifiability Improves both Parameter Estimation Accuracy and Closed-Loop Controller Robustness Guarantees

This article examines the degree to which optimizing a Rijke tube experiment can improve the accuracy of thermoacoustic model parameter estimation, thereby facilitating robust stability control. We use a one-dimensional thermoacoustic model to describe the combustion dynamics in a Rijke tube. This model contains two unknown parameters that relate velocity perturbations to heat release rate oscillations, namely, a time delay τ and amplification factor β. The parameters are estimated from experiments where the system input is the acoustic excitation from a loudspeaker and the output is the pressure response captured by a microphone. Our work is grounded in the insight that optimizing an experiment's design for higher Fisher identifiability leads to more accurate parameter estimates. The novel goal of this paper is to apply this insight in the laboratory using a flame-driven Rijke tube setup. For comparison purposes, we conduct a benchmark experiment with a broadband chirp signal as the excitation input. Next, we excite the Rijke tube at two frequencies optimized for Fisher identifiability. Repeats of both experiments show that the optimal experiment achieves parameter estimates with uncertainties at least one order of magnitude smaller than the benchmark. With smaller parameter estimate uncertainties, an LQG controller designed to attenuate combustion instabilities is able to achieve stronger robustness guarantees, quantified in terms of closed-loop structured singular values that account for parameter estimation uncertainty.

Keywords: Optimal experimental design; Fisher identifiability; uncertainty quantification; linear quadratic Gaussian; robustness guarantees

Introduction

Combustion instability is an issue in many power and propulsion systems, including gas turbines, rockets, and process furnaces. It manifests itself in the form of large-amplitude pressure oscillations that can lead to hardware vibrations and, in extreme cases, combustion system failures (Lieuwen and Yang, 2005). The cause of combustion instability is the coupling between combustor acoustics and unsteady heat release

(Lieuwen *et al.*, 1999). This coupling is problematic for modern power generation gas turbines operated with a lean-premixed combustion technique, where low-emissions operation has the potential to cause combustion instability. This is the result of the higher sensitivity of heat release to equivalence ratio with this combustion technique.

Combustion instability can be mitigated through either passive or active means. Passive mechanisms include the change of combustor acoustic characteristics or heat release dynamics. The former includes the use of acoustic damping resonators to absorb acoustic oscillations (Dupere and Dowling, 2005). The latter adjustment can be achieved either through fuel injection strategy changes (Steele *et al.*, 2000) or fuel staging techniques (Samarasinghe *et al.*, 2017). Active mitigation (Dowling and Morgans, 2005), in contrast, typically utilizes external actuation signals such as acoustic forcing (Dines, 1984; Lang, Poinsot and Candel, 1987; Annaswamy *et al.*, 2000; Gelbert *et al.*, 2012) or a secondary heat source (Seume *et al.*, 1997; S Murugappan *et al.*, 2003) to suppress the thermoacoustic instability. Regardless of the techniques of instability suppression used, the availability of an accurately parameterized model of combustion dynamics can be valuable for system design, simulation, and evaluation. Additionally, estimating the parameters of a combustion instability model more accurately has the potential to allow for closed-loop control design with stronger robustness guarantees.

Combustion instability models can either take the form of a frequency response of the combustion system (Bernier *et al.*, 2003; Epperlein, Bamieh and Åström, 2015) or be physics-based and built from combustor acoustics and heat release dynamics (Hathout *et al.*, 1998; Schuller, Durox and Candel, 2003; Heckl, 2010; Palies *et al.*, 2011). Both types of models need to be fitted to experimental data: a process known as "system identification" or "model identification". Much of the model identification literature focuses on one-dimensional combustors known as Rijke tubes (Balasubramanian and

Sujith, 2008; Heckl, 2010). This includes both electrically-driven (Heckl, 1988; Bittanti *et al.*, 2002; Selimefendigil, Sujith and Polifke, 2011; Subramanian, Sujith and Wahi, 2013; Rigas *et al.*, 2016) and flame-driven configurations (Crocco and Cheng, 1956; Dines, 1984; Vaudrey, 2001; Morgans and Dowling, 2005). The identified parameters include acoustic mode frequency (Rigas *et al.*, 2016), growth rate (Selimefendigil, Sujith and Polifke, 2011; Nair, Sarkar and Sujith, 2013; Subramanian, Sujith and Wahi, 2013; Rigas *et al.*, 2016), and time delay (Murray *et al.*, 1998; Bittanti *et al.*, 2002). The methods applied to achieve the parameter estimation include pseudospectra and Kreiss' theorem (Selimefendigil, Sujith and Polifke, 2011), linear stability analysis and nonlinear harmonic balance (Morgans and Dowling, 2005; Subramanian, Sujith and Wahi, 2013; Rigas *et al.*, 2016), describing functions (Bittanti *et al.*, 2002), least-square fitting (Koshigoe, Komatsuzaki and Yang, 1999; Vaudrey, 2001), and online identification (Koshigoe, Komatsuzaki and Yang, 1999). The uncertainties in parameter estimates determine the accuracy of a combustion dynamics model. Recent research explores different methods to quantify uncertainties in combustion instability models. This includes Monte Carlo analysis (Bauerheim *et al.*, 2014; Ndiaye *et al.*, 2015; Magri *et al.*, 2016; Silva *et al.*, 2017), adjoint perturbation theory (Mensah, Magri and Moeck, 2018), non-intrusive polynomial chaos expansion (Avdonin *et al.*, 2018), and integrated interpolation schemes (Nair, Sarkar and Sujith, 2013).

Given the importance of accurate parameter identification in a combustion model for instability control, this work poses two research questions: *First, to what extent can combustion instability experiments be designed to minimize the resulting parameter uncertainties? Second, to what extent does the improvement in combustion instability model accuracy affect the robustness of a linear quadratic Gaussian (LQG) controller in attenuating the combustion instabilities?*

This work is motivated by the above two questions. Specifically, the article focuses on the use of Fisher information analysis to quantify the best-achievable parameter estimation accuracy from Rijke tube experiments. The parameter estimate accuracy is optimized by maximizing a scalar Fisher information metric subject to constraints on the experiment's design. This metric quantifies the accuracy with which the Rijke tube's parameters can be estimated from input-output experimental data (Manchester, 2010). A classical time-delay model, the n-τ model (Dowling and Stow, 2003), is used in this work to show the utility of the Fisher information method using both theory and experiment, rather than to innovate in terms of thermoacoustic model. As such, this methodology could be extended to more complex models in the future.

Fisher information analysis provides a minimum co-variance matrix bound for the estimated parameters via the Cramér-Rao inequality (Pronzato, 2008; Forman *et al.*, 2012; Mendoza *et al.*, 2016). In this work, based on the nominal values of the estimated parameters, we can apply Fisher information analysis to assess the local identifiability of a model's parameters around the nominal values. Previous work by the authors shows, in simulation, the potential benefits of optimizing a Rijke tube experiment for Fisher identifiability (Chen *et al.*, 2019). This work provides the experimental validation of the applicability of Fisher information analysis to combustion stability experiments. The work shows that optimizing a Rijke tube experiment for Fisher identifiability furnishes tighter parameter estimates (i.e., smaller estimation uncertainties) compared to a benchmark experiment where the Rijke tube is excited using a broadband input signal. This broadband excitation is similar to traditional flame transfer function measurement methods, where flames are subjected to large ranges of individual frequencies and their response measured (Freitag *et al.*, 2006; Kim *et al.*, 2010; Palies *et al.*, 2010); these

methods are time consuming and information-heavy, making them cumbersome to use in control settings.

To the best of the authors' knowledge, such validation is a novel contribution to the combustion instability literature, where the focus has been on uncertainty quantification (Bauerheim *et al.*, 2014; Ndiaye *et al.*, 2015; Magri *et al.*, 2016; Silva *et al.*, 2017) rather than optimizing experimental designs for uncertainty minimization. A second contribution of this work is to show that the above improvement in parameter estimation accuracy makes it possible to design a closed-loop LQG combustion stability controller with stronger robustness guarantees. A control system that is designed using a simulation model of a given system is "robust" if it continues to operate in a stable and acceptable manner when implemented on the real physical system. Robustness is important in the presence of modeling uncertainties, including uncertainties in the given system's parameters. One way to achieve robustness is to design a control algorithm explicitly for robustness: a process that often involves navigating fundamental trade-offs between performance and robustness. Another way that we ensure robustness is to maximize model accuracy, thereby minimizing the discrepancies between the "simulated" and "true" combustion systems and achieving stronger robustness guarantees.

The outline of the rest of the article is as follows. The "Combustion Instability Model" section introduces both the experimental setup for a one-dimensional thermoacoustic model identification as well as the model that describes the combustion system. The "Experimental Designs for Model Identification" section presents the benchmark and optimized experimental designs for identifying the model's two key parameters. This section also compares the parameter estimation results from these two experiments. The last section, titled "Robustness of LQG Controller based on Identified

System", uses the structured singular value, μ, to analyze the robustness of an LQG controller designed for suppressing the combustion instabilities. This analysis shows the degree to which tighter parameter estimation errors can enable tighter robustness guarantees for closed-loop combustion stability control.

Combustion Instability Model

Rijke Tube Experimental Setup

The one-dimensional thermoacoustic system studied in this article is a flame-driven Rijke tube. This tube's cross-sectional view is illustrated in Fig. 1. This combustor consists of two concentric tubes. The diameters of the inner and outer tubes are $d_{inner} = 0.022m$ and $d_{outer} = 0.091m$, respectively. The outer tube is of length $L = 0.875m$. The inner tube delivers the air/fuel mixtures, and a premixed flame at equivalence ratio $\phi = 0.8$ is stabilized on a perforated plate on top of this inner tube. In the outer tube, a co-flow of air flows in the same direction as the fuel/air mixture in the inner tube. Flows within both tubes pass through ball bearings and perforated plates before entering the experiment, in order to achieve a uniform flow profile. A speaker mounted near the Rijke tube inlet provides acoustic forcing to the system. At the exit, the Rijke tube is open to the atmosphere. Thermocouples and pressure transducers are placed at discrete locations along the outer tube to measure local temperatures and pressures.

The inner tube is adjustable vertically such that the flame location can be varied, where the flame location b is defined as the length from the inlet of the outer tube to the top of the inner tube. Due to the heat release from the flame, the temperatures in the region downstream of the flame will be higher than that in the upstream region, resulting in variations in gas density, flow velocity, and sound speed.
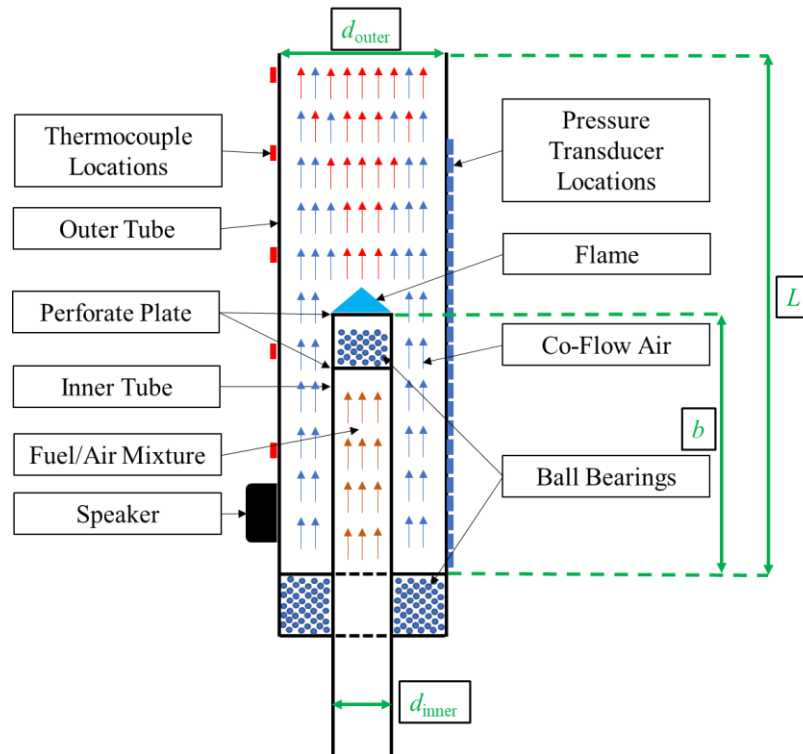
Figure 1. Cross-sectional view of the Rijke tube experimental setup

One-dimensional Thermoacoustic Model

To describe the thermoacoustic dynamics in the Rijke tube, we use a one-dimensional combustion instability model. The radial and azimuthal variations of the gas properties in the Rijke tube are small and hence neglected. The geometry of the modeled system is shown in Fig. 2. The main difference between the modeled system and the real system is the temperature distribution along the length of the Rijke tube. In the experimental setup, the temperature decays downstream of the flame due to the heat loss to the surrounding environment. In contrast, the model assumes a step temperature change across the flame, with a spatially uniform temperature T_2 in the region downstream of the flame. The temperature of the reactants upstream of the flame is T_1.
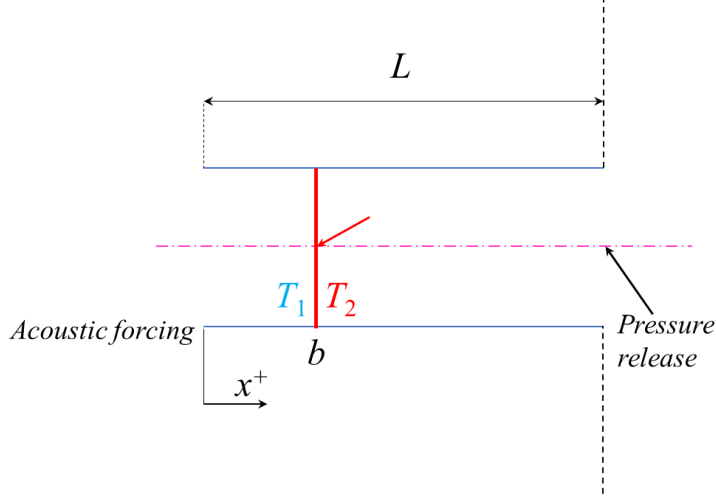
Figure 2. One-dimensional thermoacoustic model configuration

In addition to the assumption of a step temperature rise from T_1 to T_2 across the flame, we also assume an isentropic, homogeneous, and steady mean flow in the tube. Following the work of Dowling and Stow (Dowling and Stow, 2003), we describe the thermoacoustic system with linearized partial differential equations for the conservation of mass, momentum, and energy, as indicated in Eqn. (1-2).

$$\frac{\partial \rho'}{\partial t} + \bar{\rho}\frac{\partial u'}{\partial x} = 0, \bar{\rho}\frac{\partial u'}{\partial t} = -\frac{\partial p'}{\partial x} \tag{1}$$

$$\frac{\partial p'}{\partial t} = -\bar{\rho}\bar{c}^2 \frac{\partial u'}{\partial x} + (\gamma - 1)q' \tag{2}$$

These equations assume that: (i) the mean flow Mach number is significantly smaller than one (i.e., the mean flow velocity u_b is much smaller than the speed of sound $\bar{c}$); and (ii) fluctuation amplitudes in the following variables including density ρ', pressure p', velocity u', and temperature T' around the equilibrium are much smaller than the corresponding mean variables $\bar{\rho}, p_{atm}, \bar{c}$, and $\bar{\bar{T}}$, respectively.

In Eqn. (2), q' represents the fluctuation of heat release rate per unit volume and γ is the specific heat capacity ratio. We apply a linear time lag model (Crocco and Cheng, 1956), as indicated in Eqn. (3), to describe the response of the oscillating heat release per

unit area Q' to acoustic particle velocities for the acoustically compact flame, which is modeled by a spatial Dirac delta function $\delta(x - b)$.

$$q'(x, t) = Q'(t)\delta(x - b), Q'(t) = -\frac{\beta\bar{\rho}\bar{c}^2}{\gamma-1}u_1'(t - \tau) \tag{3}$$

In Eqn. (3), β is the amplification factor, representing the interaction strength between the heat release rate and velocity oscillations, and τ is time delay between the flame response and the incident velocity perturbation. The variable u_1' is the acoustic particle velocity near the upstream margin of the flame. Two boundary conditions shown in Fig. 2 are in Eqn. (4). The speaker inputs an acoustic particle velocity $u_{inlet}'(t)$ at the inlet of the Rijke tube. The outlet, in contrast, is a pressure release boundary with zero pressure oscillations.

$$u'(0, t) = u_{inlet}'(t), p'(L, t) = 0 \tag{4}$$

By manipulating Eqn. (1) and Eqn. (2), we obtain the governing non-homogeneous acoustic wave equation, as indicated in Eqn. (5).

$$\frac{\partial^2 p'}{\partial t^2} - \bar{\rho}\bar{c}^2\frac{\partial}{\partial x}\left(\frac{1}{\bar{\rho}}\frac{\partial p'}{\partial x}\right) = \frac{\beta\bar{\rho}\bar{c}^2}{\bar{\rho}_1}\delta(x - b)\frac{\partial p_1'(t-\tau)}{\partial x} \tag{5}$$

Equation (5) describes the thermoacoustic wave behavior in the Rijke tube with a flame. The source term on the right-hand side is represented by p_1' after the manipulation, which is the pressure oscillation at $x = b^-$, just upstream of the flame.

Transfer Function Representation of the Thermoacoustic System

The governing wave equation describing the thermoacoustic system's behavior is linear with respect to time, t. As a result, with the assumption of zero initial conditions, we can apply the Laplace transform to the equation and solve it analytically with the boundary

conditions specified in Eqn. (4). The solution to the differential wave equation in the s domain is pressure oscillation $P'(x, s)$ along the Rijke tube.

The input to the thermoacoustic system is the acoustic particle velocity from the speaker at the inlet and the output is the local pressure oscillation along the tube. The input particle velocity can be estimated using the two-microphone method (TMM) (Bodén and Åbom, 1986). Because the input and output variables have different units, we normalize them before calculating the system transfer function. The nominal particle velocity and pressure oscillation used for normalization are bulk flow velocity, u_b, and atmospheric pressure, p_{atm}. The definitions of the normalized transfer function, input, and output are in Eqn. (6).

$$H_n(x, s) \equiv \frac{P'_n(x,s)}{U'_n(0,s)}$$
$$P'_n(x, s) = \frac{P'(x,s)}{p_{atm}}, U'_n(0, s) = \frac{U'_0(0,s)}{u_b} \tag{6}$$

Like the output pressure distribution, the above transfer function also has different forms in the regions upstream and downstream of the flame, as shown in Eqn. (7-8).

$$H_n(x, s) = \begin{cases} \dfrac{\bar{\rho}_1 \bar{c}_1 u_b}{p_{atm}} \dfrac{(\bar{\rho}\bar{c}e_{24})e^{-\frac{x}{\bar{c}_1}s} - (\bar{\rho}\bar{c}e_{13})e^{\frac{x}{\bar{c}_1}s}}{\bar{\rho}_m\bar{c}_m e_m + \bar{\rho}_n\bar{c}_n e_n} & 0 < x \le b \\[4mm] \dfrac{(\bar{\rho}_m^2\bar{c}_m^2 - \bar{\rho}_n^2\bar{c}_n^2)e^{t_5 s}u_b\left(e^{\frac{2L-x}{\bar{c}_2}s} - e^{\frac{x}{\bar{c}_2}s}\right)}{2p_{atm}(\bar{\rho}_m\bar{c}_m e_m + \bar{\rho}_n\bar{c}_n e_n)} & b < x \le L \end{cases} \tag{7}$$

$$\begin{cases} t_1 = \dfrac{b}{\bar{c}_2} + \tau, t_3 = \dfrac{2L-b}{\bar{c}_2} + \tau, t_2 = \dfrac{2b}{\bar{c}_1} + t_3, t_4 = \dfrac{2b}{\bar{c}_1} + t_1, t_5 = \dfrac{b}{\bar{c}_1} + \tau \\[3mm] \bar{\rho}_m\bar{c}_m = \bar{\rho}_1\bar{c}_1 + (1 - \beta e^{-\tau s})\bar{\rho}_2\bar{c}_2, \bar{\rho}_n\bar{c}_n = \bar{\rho}_1\bar{c}_1 - (1 - \beta e^{-\tau s})\bar{\rho}_2\bar{c}_2 \\[3mm] e_{13} = \dfrac{\bar{\rho}_m\bar{c}_m e^{t_1 s} + \bar{\rho}_n\bar{c}_n e^{t_3 s}}{\bar{\rho}_1\bar{c}_1}, e_{24} = \dfrac{\bar{\rho}_m\bar{c}_m e^{t_2 s} + \bar{\rho}_n\bar{c}_n e^{t_4 s}}{\bar{\rho}_1\bar{c}_1} \\[3mm] e_m = e^{t_1 s} + e^{t_2 s}, e_n = e^{t_3 s} + e^{t_4 s} \end{cases} \tag{8}$$

The transfer function depends not only on experimental design variables such as flame location b, co-flow velocity u_b, sensor placement x, and excitation frequency s,

but also on the parameters to be identified: τ and β in the heat release dynamics model. For any given choice of the experimental design variables, we can estimate the two parameters by measuring the transfer function's magnitude versus frequency. To solve for the two unknown parameters, we need at least two equations based on two different transfer function magnitudes, measured at two different frequencies. If experimental data is available at a large set of excitation frequencies, one can use optimization methods to find the best fit values of the two unknown parameters.

Experiment Designs for Model Identification

We present model identification experiments for two cases with two different flame locations. The intent is to illustrate the broad applicability of this article's optimal experimental design methods. Two experimental design variables, namely, flame location and co-flow velocity, determine the temperature distribution along the Rijke tube. With different temperature distributions, the acoustic characteristics of the combustion system are also different. Thus, our examination of two different cases with different flame locations makes it possible to illustrate the benefits of optimal experimental design for combustors with different acoustic characteristics.

We characterize the temperature distribution inside the tube with experimental measurements obtained via K-type thermocouples. The gas temperature downstream of the flame decreases in both the positive axial and radial directions due to the co-flow's existence and heat loss to the surrounding environment. To match the simplified step distribution in the model in Fig. 2, we average the downstream temperature volumetrically to a constant. The resulting step temperature distributions along the Rijke tube for the two cases are summarized in Table 1. The heat release remains constant for the two cases because of the same combustion equivalence ratio. The downstream

temperature changes because of the changes in flame location: the higher flame location causes a slight increase of the temperature by approximately 4°C in the product region because distance available for heat loss to the environment is shorter when the total length of the Rijke tube is fixed.

Table 1. Cases with characterized temperature distribution

Variable	Case 1	Case 2
b [m]	0.3	0.4
u_b [m/s]	2	2
T_1 [°C]	21.0	21.0
T_2 [°C]	67.1	71.0

Experimental Design

For each one of the two experimental cases, we identify the parameters $\hat{\tau}$ and $\hat{\beta}$ from measurements of the system's transfer function magnitudes at multiple frequencies. As defined in Eqn. (6), we add an acoustic signal as input to the system from a speaker and measure the output pressure oscillations along the Rijke tube using PCB 113B24 series pressure transducers. We collect the pressure signal using a dSPACE DS1104 board at a specified sampling rate $f_s = 20\ kHz$ and recording duration t_d. As indicated in the sub-sections "Benchmark – Broadband Frequency Response" and "Optimal – Two-Frequency Response", data acquisition time lengths are 20 seconds and 4 seconds for the benchmark case and optimal case, respectively. The measurement uncertainty of the pressure transducers is $\sigma_p = 7\ Pa$ and the number of repeated measurements is $N_{rp} = 50$ ($N_{rp} = 4\frac{Z^2\sigma_p^2}{W^2}$) to ensure sufficient statistical power with 95% confidence and $\pm 2\sigma_p$ error bounds ($W = 4$) in measuring the output pressure oscillations.

Benchmark - Broadband Frequency Response

Thermoacoustic systems are typically identified by measuring the frequency-domain response of the system at a range of frequencies (Epperlein, Bamieh and Åström, 2015). Based on the measured frequency response, researchers usually choose a rational transfer function with an appropriate order to represent the identified system. Then they determine the coefficients in the transfer function expression using the least-mean-squares (LMS) method over the frequency range of interest. In our work, we apply this method as a benchmark to identify the two parameters. The frequency response range we select for the benchmark cases is from 400 Hz to 800 Hz, which avoids low frequencies that can blow off the flame easily but still covers the third and fourth acoustic modes of the system. The frequency of the input signal varies linearly for 20 seconds, at a variation rate of 20 Hz/s, and a fast Fourier transform is used for obtaining an empirical transfer function from the resulting time series with a frequency resolution of 5 Hz. Then there are 81 points in showing the frequency response of the transfer function magnitude in the frequency range from 400 Hz to 800 Hz, with an increment of frequency 5 Hz. For the sensor placement, the optimal location for the pressure transducer is the location closet to the Rijke tube inlet, which is concluded in the following sub-section "Optimal Experimental Design – Two-Frequency Response".

Optimal Experimental Design – Two-Frequency Response

In the previous sub-section, we apply a broad band signal as the input to identify the thermoacoustic model parameters in a Rijke tube combustion system. As a comparison, we conduct an optimal model identification experiment based on the designs achieved from Fisher information analysis. The optimization problem aims to minimize the resulting parameter estimation uncertainties. We apply Fisher identifiability analysis to obtain a quantification of the lower bound of parameter estimation uncertainty. In this

case, the determinant of the Fisher information matrix is the scalar objective for optimization, subject to constraints on input frequencies and sensor placement along the Rijke tube.

Fisher identifiability analysis has been commonly used to estimate uncertainties of system characteristics such as initial conditions, state variables, or certain parameters when measurements are limited (Sharma and Fathy, 2014; Mendoza *et al.*, 2016). Prior to using Fisher identifiability analysis, we make the following assumptions. First, we assume a constant variance of output pressure measurements no matter where the pressure transducer is placed and what excitation frequencies are used. The second assumption is that there is no uncertainty in the measurement of input particle velocity. As a result, the magnitude of the measured system transfer function, which is defined as the ratio of pressure to particle velocity, is only affected by uncertainties from pressure magnitude measurement. Third, we assume that the estimation process furnishes unbiased estimates of the unknown parameters ($\hat{\tau}_0 = \tau_{0,true}, \hat{\beta}_0 = \beta_{0,true}$). Lastly, we assume independent, identically distributed errors in measuring the transfer function magnitude, as indicated in Eqn. (9).

$$p\left(\left|H_{n,m}(x,s)\right|;\widehat{\boldsymbol{\theta}}\right) = \frac{1}{\sqrt{2\pi\sigma^2}}e^{-\frac{1}{2\sigma^2}\left[\left|H_{n,m}(x,s)\right|-G(x,s,\widehat{\boldsymbol{\theta}})\right]^2} \tag{9}$$

The subscript "*m*" in $H_{n,m}(x,s)$ denotes measurements. The function $G\left(x,s,\widehat{\boldsymbol{\theta}}\right)$ describes the modelled transfer function magnitude $|H_n(x,s)|$ based on the estimated parameter vector $\widehat{\boldsymbol{\theta}}$, with definitions in Eqn. (10) and Eqn. (11).

$$\widehat{\boldsymbol{\theta}} = \begin{bmatrix} \hat{\tau}_n \\ \hat{\beta}_n \end{bmatrix} \tag{10}$$

$$\hat{\tau}_n = \frac{\hat{\tau}}{\hat{\tau}_0}, \hat{\beta}_n = \frac{\hat{\beta}}{\hat{\beta}_0}, \hat{\tau}_0 \equiv \frac{b_0}{u_0}, \hat{\beta}_0 \equiv 1 \tag{11}$$

In the thermoacoustic model, the two estimated parameters have different units and orders of magnitude. To make them comparable, we define a normalized parameter estimates vector $\widehat{\boldsymbol{\theta}}$ in Eqn. (10) with each parameter normalized by its corresponding nominal value. The definitions of the nominal values are in Eqn. (11). In this equation, the nominal flame location, b_0, is 0.25 m and the nominal bulk flow velocity, u_0, is the same as co-flow velocity u_b.

In Eqn. (9), the probability density function represents the likelihood that observed discrepancies between the estimated and measured system transfer functions are mere outcomes of measurement noise. Maximum likelihood estimation methods, including least squares estimation, attempt to maximize this likelihood function. The idea is to minimize systematic errors in system identification by finding those parameter estimates for which the estimation residuals are most likely to be consequences of measurement noise. When such maximum likelihood estimation is performed, the expected value of the Hessian of the likelihood function with respect to the unknown parameters is called the Fisher information matrix, $F(\widehat{\boldsymbol{\theta}})$. Intuitively, the larger this expected value, the "sharper" the likelihood function will be around the maximum likelihood estimation results, which implies more accurate parameter estimation. This intuitive result is formalized mathematically through the Cramér-Rao theorem, which states that the best-achievable unbiased parameter estimation covariance is equal to the inverse of the Fisher information matrix, assuming this inverse exists. Stated mathematically, the Cramér-Rao lower bound (CRLB) is given by Eqn. (12).

$$\text{var}(\widehat{\boldsymbol{\theta}}) \geq \left[-E\left[\frac{\partial^2 \ln p(|H_{n,m}|;\widehat{\boldsymbol{\theta}})}{\partial \widehat{\theta}_i \partial \widehat{\theta}_j} \right] \right]^{-1} \tag{12}$$

The Fisher information matrix is strongly influenced by the sensitivity of the likelihood function to the underlying unknown parameters. Intuitively, the more sensitive

the likelihood function is to the underlying unknown parameters, the more accurately they can be determined via maximum likelihood estimation. Mathematically, this insight translates into the following relationship between the Fisher information matrix and the sensitivity of the likelihood function with respect to the underlying parameters:

$$\left[F(\widehat{\boldsymbol{\theta}})\right]_{ij} = -E\left[\frac{\partial^2 \ln p(|H_{n,m}|;\widehat{\boldsymbol{\theta}})}{\partial \widehat{\theta}_i \partial \widehat{\theta}_j}\right] = -E\left[\left(\frac{\partial \ln p(|H_{n,m}|;\widehat{\boldsymbol{\theta}})}{\partial \widehat{\theta}_i}\right)\left(\frac{\partial \ln p(|H_{n,m}|;\widehat{\boldsymbol{\theta}})}{\partial \widehat{\theta}_j}\right)^T\right] \quad (13)$$

Given the definition of the likelihood function, one can rewrite the Fisher information matrix in terms of the thermoacoustic system's transfer function $G(x, s, \widehat{\boldsymbol{\theta}})$, as follows:

$$F(\widehat{\boldsymbol{\theta}}) = \frac{1}{\sigma^2}\begin{bmatrix} F_{11} & F_{12} \\ F_{21} & F_{22} \end{bmatrix} \quad (14)$$

$$
\begin{aligned}
F_{11} &= \sum_{i=1}^{N} \frac{\partial G_{j\omega_i}(x,s,\widehat{\boldsymbol{\theta}})}{\partial \widehat{\tau}_n} \cdot \frac{\partial G_{j\omega_i}(x,s,\widehat{\boldsymbol{\theta}})}{\partial \widehat{\tau}_n} \\
F_{12} = F_{21} &= \sum_{i=1}^{N} \frac{\partial G_{j\omega_i}(x,s,\widehat{\boldsymbol{\theta}})}{\partial \widehat{\tau}_n} \cdot \frac{\partial G_{j\omega_i}(x,s,\widehat{\boldsymbol{\theta}})}{\partial \widehat{\beta}_n} \\
F_{22} &= \sum_{i=1}^{N} \frac{\partial G_{j\omega_i}(x,s,\widehat{\boldsymbol{\theta}})}{\partial \widehat{\beta}_n} \cdot \frac{\partial G_{j\omega_i}(x,s,\widehat{\boldsymbol{\theta}})}{\partial \widehat{\beta}_n}
\end{aligned} \quad (15)
$$

In Eqn. (15), ω is the acoustic excitation frequency, N is the number of model identification tests, each test occurring at an individual frequency. According to Eqn. (12), the covariance matrix $C_{\widehat{\theta}}$ quantifying the parameter estimates uncertainties is no smaller than the Fisher information matrix inverse, as expressed in Eqn. (16).

$$C_{\widehat{\theta}} \geq F^{-1}(\widehat{\boldsymbol{\theta}}) = \frac{\sigma^2}{F_{11}F_{22}-F_{12}^2}\begin{bmatrix} F_{22} & -F_{12} \\ -F_{21} & F_{11} \end{bmatrix} \quad (16)$$

Minimizing this lower bound will, in theory, furnish better (i.e., more accurate) bounds on the best-achievable parameter estimation accuracy levels for the two unknown combustion model parameters. This explains the frequent use of Fisher information

maximization as a tool for optimal experimental design in the literature. One common optimization metric is the determinant of the Fisher information matrix, but other optimization metrics are possible, including maximizing the trace and/or eigenvalues of this matrix (Mehra, 1974; Pronzato, 2008), respectively. This article uses D-optimality, i.e., the optimization of the determinant of the Fisher information matrix, as its optimal experimental design criterion. This determinant is given by Eqn. (17) below:

$$\det(\boldsymbol{F}) = \frac{1}{\sigma^4}\left(F_{11}F_{22} - F_{12}^2\right) = \frac{1}{\sigma^4}\left(\frac{\partial G_{j\omega_1}}{\partial \hat{\tau}_n}\frac{\partial G_{j\omega_2}}{\partial \hat{\beta}_n} - \frac{\partial G_{j\omega_2}}{\partial \hat{\tau}_n}\frac{\partial G_{j\omega_1}}{\partial \hat{\beta}_n}\right)^2 \tag{17}$$

In Eqn. (17), the Fisher information matrix is calculated based on two excitation frequencies ω_1 and ω_2. The Fisher information matrix determinant depends not only on the case definition parameters - flame location b and co-flow velocity u_b, but also on the experimental design variables - acoustic excitation frequency f_{ex}, and sensor placement x. This article particularly considers the optimization of the parameter estimation accuracy by varying the following key experimental design variables: excitation frequencies f_{ex} and sensor placement x.

We describe the experimental design optimization problem with the statement in Eqn. (18). The objective of the optimization is to maximize the determinant of the Fisher information matrix, where G is the modeled transfer function magnitude based on the estimated parameters, $\hat{\tau}_n$ and $\hat{\beta}_n$. The subscript "prior" refers to the nominal parameter values obtained from prior work in the literature (Dowling and Stow, 2003).

$$\max_{\omega_1,\omega_2,x} \det(\boldsymbol{F}) = \frac{1}{\sigma^4}\left(\frac{\partial G_{j\omega_1}}{\partial \hat{\tau}_n}\frac{\partial G_{j\omega_2}}{\partial \hat{\beta}_n} - \frac{\partial G_{j\omega_2}}{\partial \hat{\tau}_n}\frac{\partial G_{j\omega_1}}{\partial \hat{\beta}_n}\right)^2$$

$$subject\ to \begin{cases} G_{j\omega_{i_f}}\left(x,\hat{\tau}_n,\hat{\beta}_n\right) = \left|H_n\left(x,j\omega_{i_f},\hat{\tau}_n,\hat{\beta}_n\right)\right| \\ \hat{\tau}_n = \hat{\tau}_{n,prior}, \hat{\beta}_n = \hat{\beta}_{n,prior} \\ \omega_{i_f} = 2\pi f_{i_f}, i_f \in \{1,2\} \\ 400Hz \leq f_{1,2} \leq 800Hz, f_{1,2} \in \mathbb{Z} \\ |f_1 - f_2| \geq \min_{m_f,n_f \in \{1,2,3,4\}}\left\{\left|f_{m_f} - f_{n_f}\right|\right\} \\ x = x_{\min} + i_x \cdot \Delta x, x_{\min} = 0.041m \\ \Delta x = 0.026m, i_x \in \left\{0,1,\dots,\left\lfloor\frac{b-0.05}{\Delta x}\right\rfloor\right\} \end{cases} \quad (18)$$

The excitation frequency constraint between 400 and 800 Hz is derived from the fact that longitudinal instabilities in gas turbine technologies are typically found in this range. Additionally, this frequency range covers two acoustic modes of the thermoacoustic system, which are the third and fourth modes near 500 Hz and 700 Hz. An additional frequency constraint is related to the difference between the two test frequencies, where f_{m_f} and f_{n_f} represent the m_f^{th} and n_f^{th} acoustic modes, respectively. This means that the difference between the two excitation frequencies should be at least larger than the minimum difference between any two of the first four acoustic modes, which guarantees that the two frequencies are distinct. Constraints on sensor placement are dependent on the geometry of the experiment; the closest placement to the Rijke tube inlet is at 0.041 m ($x_{\min}$), and it is better to place the sensor upstream of the flame with a distance of at least 5 cm avoiding high temperature radiation on the sensor.

Parameter Estimates

Benchmark - Broadband Frequency Response

With time series data acquisition of both input acoustic particle velocity and output pressure, we apply the fast Fourier transform to achieve the frequency response of the system as the ratio between the normalized pressure spectrum $P_n(\omega)$ and normalized

acoustic velocity spectrum $U_n(\omega)$. The definitions of the normalized input and output are the same as the definitions in Eqn. (6). Fig. 3 shows one of the repeats of the identified frequency responses in the two benchmark cases. The co-flow velocity is 2 m/s for both cases and the flame locations are 0.3 m and 0.4 m. With a chirp signal over frequency range of 400 to 800 Hz, we capture the third and fourth acoustic resonance modes of the system. As mentioned earlier, different flame locations cause differences in temperature distribution and different acoustic characteristics as a result, which can be seen from the difference of the two modes between the two cases in Fig. 3. The case with a higher flame location generates a fourth mode approximately 20 Hz lower than that with a lower flame location. This difference in the system transfer function will be reflected by different groups of parameters we need to identify.
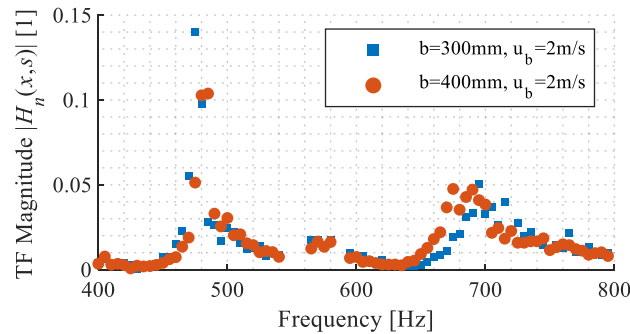

Figure 3. Frequency response of the system transfer function magnitude from a broadband chirp signal input

Based on the measured transfer function magnitudes, we minimize the root-mean-squares (RMS) of the errors between estimated and measured transfer functions to identify the parameters $\hat{\tau}$ and $\hat{\beta}$ at the frequencies displayed in Fig. 3. The parameter estimation is stated as the optimization problem in Eqn. (19).

$$\min_{\hat{\tau},\hat{\beta}} \Delta|H_n(x,s)| = \sqrt{\frac{1}{N_f}\sum_{i_f=1}^{N_f}\left[\left|H_{m,i_f}(x)\right| - G_{i_f}(x,\hat{\tau},\hat{\beta})\right]^2}$$

$$subject\ to\ \begin{cases} 11ms \le \hat{\tau} \le 12ms, 0.1 \le \hat{\beta} \le 5 \\ \Delta f = 5Hz, N_f = \frac{(800-400)Hz}{\Delta f} + 1 \\ \left|H_{m,i_f}(x)\right| = \frac{P_n\left(x,\omega_{i_f}\right)}{U_n\left(x,\omega_{i_f}\right)} \\ G_{i_f}(x,\hat{\tau},\hat{\beta}) = \left|H_n\left(x,j\omega_{i_f},\hat{\tau},\hat{\beta}\right)\right| \end{cases} \quad (19)$$

The objective of this optimization problem $\Delta|H_n(x,s)|$ is the root mean square of the transfer function magnitude difference between experimental measurements $\left|H_{m,i_f}(x)\right|$ and modeling results $G_{i_f}(x,\hat{\tau},\hat{\beta})$ based on estimated parameters. The ranges of the estimated parameters $\hat{\tau}$ and $\hat{\beta}$ are 11 to 12 ms and 0.1 to 5, respectively. In the literature (Dowling and Stow, 2003), it was suggested that the range of β is from 0 to 10, τ is typically the convection time from fuel injection to its combustion. We observed periodic distributions of time delay estimates and select the current range based on our experimental setup. The smaller range of β is selected because we found there are no estimated values of β greater than 5 in the initial estimation with a larger range from 0 to 10.

The parameter estimation problem in Eqn. (19) is non-convex because of the periodic dependence of the transfer function magnitude on the time delay in acoustic systems. There exist multiple local optimal parameter groups to match the measured transfer function magnitudes. So, we apply a genetic algorithm (GA) solver to find the estimates of time delay $\hat{\tau}$ and amplification factor $\hat{\beta}$. The genetic algorithm uses the settings outlined in Table 2. Fig. 4 shows the distribution of the estimated time delay $\hat{\tau}$ and amplification factor $\hat{\beta}$ from 50 repeated experiments in the two cases.

Table 2. GA settings for parameter estimates in the benchmark case

Options	Values
Generation number	300
Population size	2000
Crossover fraction	0.85
Crossover function	crossoverarithmetic
Selection function	selectionroulette
Function tolerance	0.001
Mutation function	mutationadaptfeasible
Computational time [s]	185

The bottom two histograms in Fig. 4 show the distribution of the RMS difference between modeled and measured non-dimensional transfer function magnitudes. The RMS values of the difference for the two cases are mainly around 0.02, which are at the same order of magnitude as the absolute normalized transfer function magnitude, as shown in Fig. 3. This indicates that the parameter estimation based on a chirp signal excitation does not ensure a good accuracy.
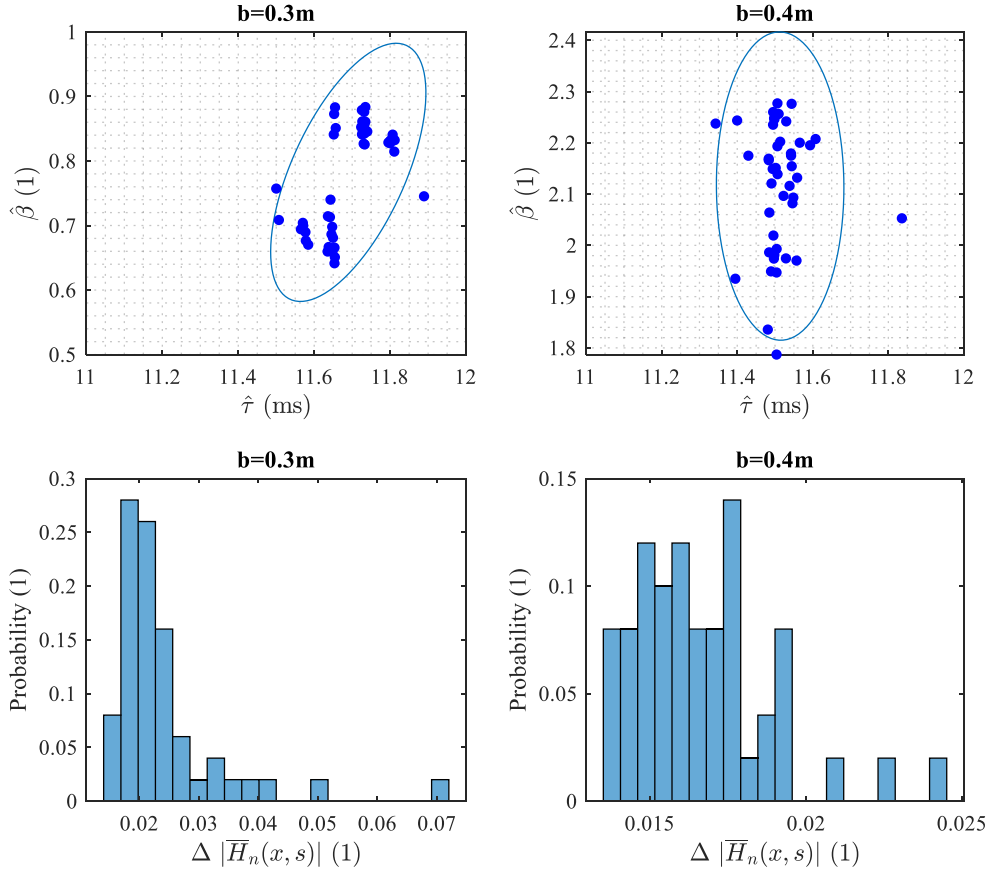
Figure 4. Parameter estimates from a broadband chirp signal in the benchmark case

The top two subplots in Figure 4 show the distribution of the two estimated parameters for the two cases, separately. A 95% confidence ellipse is also plotted to show the covariance of the two estimated parameters. The ellipse in case 1 with $b = 0.3$ m is slightly more inclined compared with that in case 2 with $b = 0.4$ m, which means that the two parameters are more correlated in cases 1 than those in case 2. For both cases, the standard deviations of amplification factor estimate $\hat{\beta}$ are around 0.4. The standard deviations of time delay estimate $\hat{\tau}$ are slightly different between the two cases. For the case with lower flame height at 0.3 m, the time delay estimate $\hat{\tau}$ achieves a larger standard deviation of 0.25 ms compared with the standard deviation of 0.07 ms in the case with higher flame height. Considering the dimensionless uncertainties normalized by the

estimated nominal parameter values $\hat{\beta}_0 = 1.5$ and $\hat{\tau}_0 = 11.5\ ms$, the standard deviation of the estimated time delay is at least one order of magnitude smaller than that of the estimated amplification factor. This difference implies that the system's transfer function magnitude has a stronger dependence on time delay than amplification factor, as indicated by Figure 5 in the authors' previous work (Chen *et al.*, 2019), and other works earlier in the literature (Venkataraman *et al.*, 1999; Lieuwen *et al.*, 2001).

Optimal Experimental Design - Two-Frequency Response

In the last sub-section, we apply a chirp signal as an input to identify the thermoacoustic model parameters in a Rijke tube combustion system. The large difference between the experimentally-observed and modeled transfer function magnitudes indicates inaccurate parametric identification in this benchmark case. As a comparison, we conduct an optimal model identification experiment based on the optimization process outlined in section 3.1.2. To make a more direct and fair comparison between the benchmark and optimal experimental designs, we do not use the nominal parameters identified from benchmark case as the prior nominal values for optimal experimental design, otherwise we will have different prior information between benchmark and optimal cases. Instead, we start with the same prior information as that in benchmark case and adopt the nominal values of the two parameters from the current literature as the reasonable prior information of the system we work on. For experimental design optimization, the prior nominal values of the two parameters in the literature (Dowling and Stow, 2003) are: $\beta_0 = 0.5$ and $\tau_0 = 2\ ms$. In the Fisher information matrix determinant optimization with prior nominal values of the two parameters, we achieve an optimal experimental design for the thermoacoustic model identifiability in the optimal case. Because both the excitation frequencies and sensor placements are discretized with finite numbers, we apply a grid

search method to achieve the optimal combination of the three design variables that leads to the largest Fisher information matrix determinant.

The experimental design variables for the two cases are shown in Table 3. The two optimal excitation frequencies in the two cases are close to the third and fourth acoustic modes in the system. At the two optimal frequencies, we achieve higher signal-to-noise ratios when measuring the magnitude of the frequency response, which helps to decrease the parameter estimate uncertainties. The optimal sensor location is always at 0.041 m, which is the sensor placement closest to the Rijke tube inlet. This optimal sensor placement is located near the acoustically closed boundary where the acoustic reflection coefficient is nearly 1, resulting in a pressure anti-node with highest oscillation amplitude.

After achieving the optimal experimental designs, we implement them in the laboratory. We apply two sinusoidal waves with two frequencies as the input and measure the output pressure at optimal sensor placement to estimate the two parameters of the thermoacoustic model. The data acquisition takes four seconds for a single repetition and we use the same number of repetitions as the benchmark case (namely, 50 repetitions) in order to achieve a fair comparison of results.

Table 3. Optimal experimental design for thermoacoustic model identifiability

Variable	Case 1	Case 2
$f_{ex,1}$ [Hz]	501	525
$f_{ex,2}$ [Hz]	710	726
x_0 [m]	0.041	0.041

We apply the same optimization technique as in the benchmark case to estimate the two parameters. The only difference lies in number of frequencies in the objective function (namely, two frequencies instead of 81). To solve the optimization problem, we

also apply a genetic algorithm with the same settings as in the benchmark case in Table 2. The computational time for the optimal case is approximately 18 seconds for one repetition, which is nearly 10% of that of the benchmark case due to the reduction in the number of excitation frequencies. In each case, 50 repetitions of the model identification experiments generate 50 groups of the two parameter estimates.
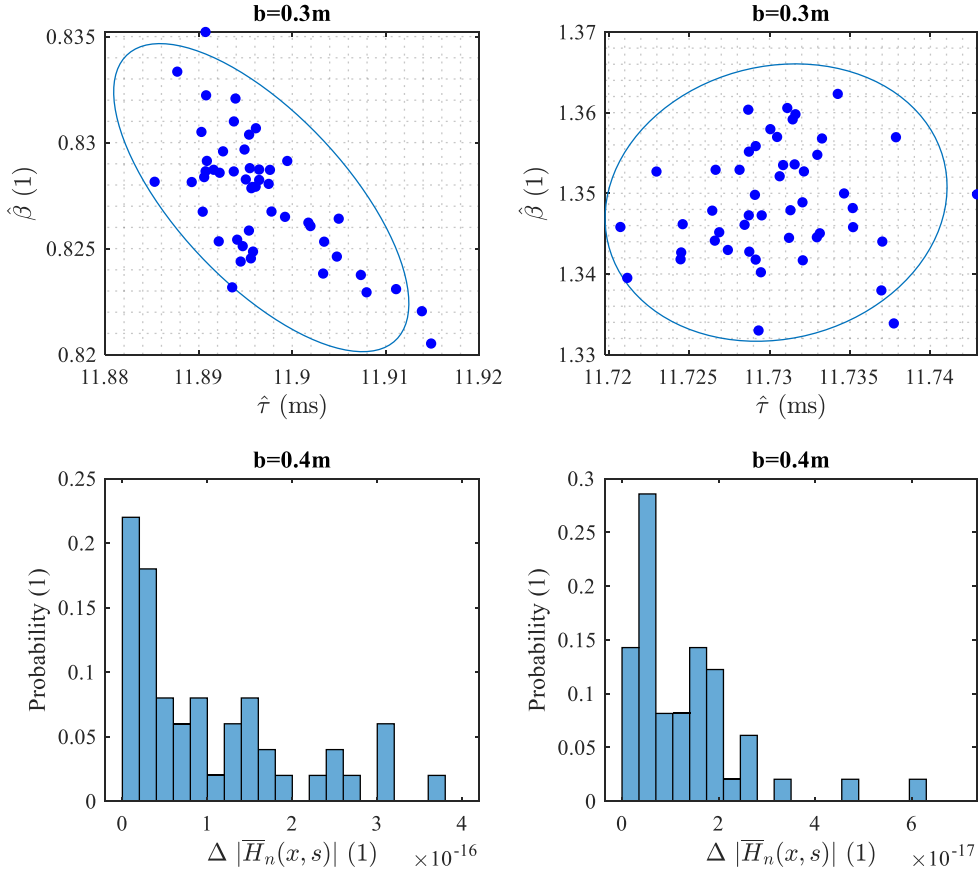

Figure 5. Parameter estimates from the optimal experimental design

The two histograms in Figure 5 provide the RMS of the difference between modeled and measured transfer function magnitudes in the two cases, where the differences are both close to zero. This means that the parameter estimates accurately describe the combustion instability in the Rijke tube for the two cases. We show the distribution of the estimated parameters in the top two subplots in Fig. 5. A 95%

confidence ellipse is also included to show the covariance of the two estimated parameters. Nominal values of the estimated time delay $\hat{\tau}_0$ are between 11 and 12 ms for both cases. However, changing the flame location from 0.3 m to 0.4 m significantly impacts the amplification factor $\hat{\beta}_0$, due to the relative position change of the flame to the pressure node. Whether the heat release location is near the pressure node/anti-node affects the interaction strength between the oscillations of heat release rate and acoustic waves. In terms of the estimation accuracy, the standard deviations of both amplification factor $\hat{\beta}$ and $\hat{\tau}$ are both on the order of 10^{-3}. The uncertainty levels in estimating $\hat{\beta}$ and $\hat{\tau}$ are comparable, in contrast to the benchmark experiments, where $\hat{\beta}$ was estimated with significantly lower accuracy levels. A detailed summary of both nominal values and variances of the parameter estimates from benchmark and optimal experimental designs is presented in the following section.

Parameter Estimates Comparison

Table 4 summarizes the parameter estimation accuracies from all experiments conducted in this work. The nominal values of the parameter estimates are similar between the optimal and benchmark cases. The optimal experimental design improves the estimate accuracy by at least one order of magnitude compared to the benchmark cases, especially for the amplification factor. The method of optimizing experimental design for parameter estimates has two main advantages. First, experimental time is significantly reduced from 20 to 4 seconds, with a commensurate reduction in the computational time for parameter estimation. Second, optimal experimental design improves the accuracy of parameter estimates by one order of magnitude at least.

Table 4. Summary of parameter estimates in benchmark and optimal cases

Nominal Value	Case 1	Case 2

	Case 1	Case 2
$\hat{\beta}_{Benchmark}$ [1]	0.782	2.116
$\hat{\beta}_{Optimal}$ [1]	0.827	1.337
$\hat{\tau}_{Benchmark}$ [ms]	11.690	11.514
$\hat{\tau}_{Optimal}$ [ms]	11.897	11.724
STD	**Case 1**	**Case 2**
$\hat{\beta}_{Benchmark}$ [1]	0.082	0.123
$\hat{\beta}_{Optimal}$ [1]	0.003	0.007
$\hat{\tau}_{Benchmark}$ [ms]	0.084	0.069
$\hat{\tau}_{Optimal}$ [ms]	0.0065	0.0043

Robustness of LQG Controller based on Identified System

The goal of combustion instability control is to attenuate the pressure oscillation amplitude when the instability grows. We can apply optimal control with the pressure oscillation amplitude as the cost to minimize. Linear quadratic Gaussian (LQG) control is one of the optimal control techniques that can be used for combustion stability control in the presence of noisy measurement and actuation signals. There have been a number of applications of LQG control technique to attenuate the combustion instability in the literature (Hathout *et al.*, 1998; Annaswamy *et al.*, 2000; S. Murugappan *et al.*, 2003).

LQG controllers are optimal, in the sense of minimizing combustion instability oscillations assuming that the system models used for LQG design are accurate. This optimality comes at a price in terms of robustness: an LQG controller designed to stabilize a combustion process for a nominal plant may become unstable if the dynamics of the true plant are sufficiently different from nominal. One pathway for ensuring greater robustness is to design a control algorithm explicitly for robustness, using methods such as loop transfer recovery (LTR), H_∞ control, etc. Optimal experimental design offers an

important complementary pathway: by reducing parameter estimation errors, one can reduce the uncertainty in the dynamics of the nominal plant model used for control design. Regardless of the control design scheme used, LQG or otherwise, reductions in plan model uncertainties lead to greater mathematical assurances (i.e., "robustness guarantees") for the stability of the resulting controller in the presence of uncertainty. The goal of this section is to examine this important connection between optimal experimental design and combustion stability controller robustness.

Specifically, we analyze the robustness guarantees of an LQG controller designed to attenuate the combustion instability with model uncertainties. The model used for controller design is identified with the parameters $\hat{\beta}$ and $\hat{\tau}$ estimated from the last section. Before designing the LQG controller for the nominal plant, we reduce the order of the original time-delayed thermoacoustic model. Model order reduction generates approximation errors. However, when we analyze the controller's robustness, we only consider the uncertainties from parameter estimation and neglect the uncertainties caused by order reduction errors. We evaluate the robustness of the controller using the structured singular values of the closed-loop system with the LQG controller designed for the nominal plant. The smaller parameter estimation uncertainties achieved from the optimal experimental design should help to design an optimal controller with stronger robustness guarantees compared to the benchmark case.

Model Order Reduction

The model parameters for the LQG controller design and robustness analysis are from Table 4. We apply multipoint Padé approximation (Celik *et al.*, 1995) on the identified transfer functions to obtain order-reduced models with finite dimensions. In the approximation, the moment-matching points are near the four acoustic modes and the

order of each moment matching point is two, which means that the approximated model has an order of eight. The frequencies of the matching points are 108, 311, 535, and 709 Hz for case 1 and 110, 313, 477, and 732 Hz for case 2. As indicated in Fig. 6, the approximated models keep the original systems' characteristics with small transfer function magnitude differences, especially near the four acoustic modes. With the nominal transfer function magnitude around 0.15, the relative differences of the approximated systems to original systems are not greater than 10% at most frequencies.
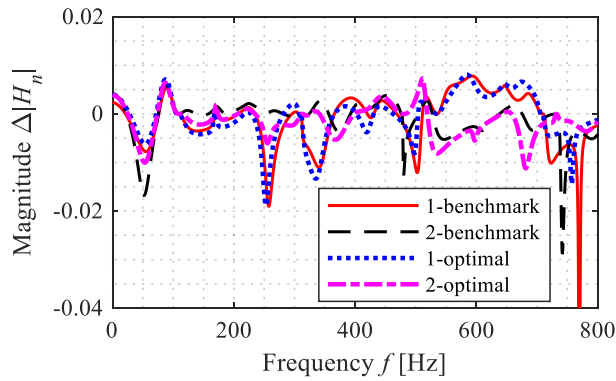

Figure 6. Magnitude error of Padé approximation for the original transfer functions in both benchmark and optimal cases

LQG Design and Uncertainty Matrix

Optimal LQG Controller Design

The approximated models maintain the instability characteristics at the same modal frequencies as the original models. To suppress the combustion instabilities at those frequencies, we design an LQG controller based on the nominal plant after the multipoint Padé approximation. The cost function of the LQG controller design J is defined as Eqn. (20).

$$J = \int_0^\infty [x^T, u^T] Q_{xu} \begin{bmatrix} x \\ u \end{bmatrix} dt \qquad (20)$$

The weighting matrix Q_{xu} determines the tradeoff between inputs u and states x. The definition of Q_{xu} depends on the objective of the LQG controller and we aim to suppress the pressure oscillation, also as the output of the system. So, the definition of Q_{xu} is in Eqn. (21).

$$Q_{xu} = \begin{bmatrix} C^T C & \mathbf{0} \\ \mathbf{0} & R \end{bmatrix}, \ Q_{wv} = \begin{bmatrix} w \\ v \end{bmatrix} \cdot [w^T \quad v^T] = \begin{bmatrix} ww^T & \mathbf{0} \\ \mathbf{0} & vv^T \end{bmatrix} \tag{21}$$

We assume that no correlation exists between states and inputs, so the off-diagonal elements are $\mathbf{0}$ in matrix Q_{xu}. The bottom-right element R is selected to be 1 and C in the upper-left element is the output matrix in the state space form. In this equation, another weighting matrix Q_{wv} describes the covariance from the two noise sources: w for processing noise and v for measurement noise. The intensities of Gaussian white noise sources w and v are selected to be 7×10^{-5}, which is the uncertainty level of the normalized pressure measurement, approximately the ratio of the pressure transducer measurement uncertainty $7 \ Pa$ to the atmospheric pressure $1.013 \times 10^5 \ Pa$. The two noise sources are assumed to be statistically independent.

Multiplicative Uncertainty Weighting Matrix

As illustrated in Table 4, both parameters have uncertainties from the system identification tests. Since we neglect modeling errors from the Padé approximation, we quantify the model's uncertainty by evaluating the relative difference between the perturbed model G_p and nominal model G_0. The definition of the multiplicative uncertainties is in Eqn. (22).

$$\Delta_u = \frac{G_p - G_0}{G_0}, \ G_p = (1 + \Delta_u)G_0 \tag{22}$$

The multiplicative uncertainty Δ_u can be replaced by an upper bound weighting matrix $W_u(s)$, as in Eqn. (23).

$$\Delta_u(s) = W_u(s)\Delta, \ \|\Delta\|_\infty \leq 1 \tag{23}$$

Assuming both parameters have an uncertainty of one standard deviation level, that $\hat{\tau}$ varies within $[\hat{\tau}_0 - \sigma_{\hat{\tau}}, \hat{\tau}_0 + \sigma_{\hat{\tau}}]$ and $\hat{\beta}$ varies within $[\hat{\beta}_0 - \sigma_{\hat{\beta}}, \hat{\beta}_0 + \sigma_{\hat{\beta}}]$, the multiplicative weighting matrix W_u has a frequency response indicated in Fig. 7 for the two cases with both benchmark and optimal system identification conditions. Similar to the parameter estimate uncertainties comparison in Table 4, the multiplicative uncertainty weights for the benchmark cases are about one order of magnitude higher than those for optimal cases.
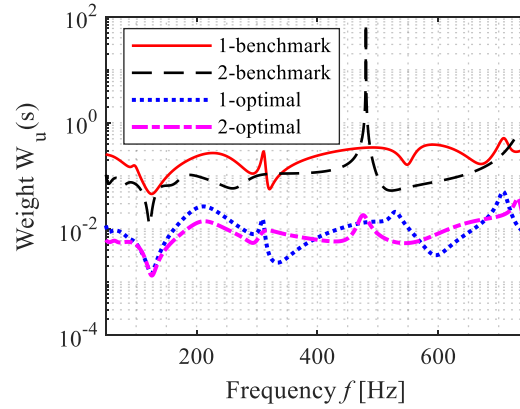

Figure 7. Frequency dependence of the multiplicative uncertainty weight $W_u(s)$

Robustness of LQG Controller

Structured Singular Value

The multiplicative transfer function H_{mult} has the corresponding form in Eqn. (24).

$$H_{mult} = \begin{bmatrix} 0 & W_u \\ G_0 & G_0 \end{bmatrix} \tag{24}$$

The output y and input u are connected by the feedback LQG controller. The uncertain closed-loop system M with feedback control is achieved with a lower linear fractional transform as in Eqn. (25).

$$M = F_l\big(H_{mult}, -K_{lqg}\big) \qquad (25)$$

The robustness of the controller can be evaluated by the structured singular value $\mu_\Delta(M)$ of the closed-loop system M, which describes the gain from disturbance to error. We apply the MATLAB robust control toolbox to calculate the structured singular values.

LQG Robustness Comparison

In this section, we compare the robustness of the LQG controller, represented by the structured singular value of the closed-loop system, between models identified from benchmark and optimal conditions. The frequency response of the singular value μ is illustrated in the Fig. 8.
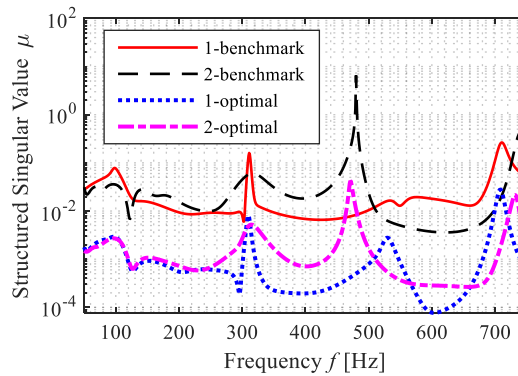

Figure 8. Frequency response of LQG robustness metric structured singular value $\boldsymbol{\mu}$

The structured singular value of a closed-loop dynamic system (i.e., a system with an active controller) is a function of frequency, as shown in Figure 8. The magnitude of the structured singular value is an indication of (the lack of) robustness: a larger

magnitude corresponds to weaker robustness guarantees. If the structured singular value exceeds 10^0, at any frequency, for a given closed-loop system, this is an indication of very poor controller robustness. In such a case, uncertainties in the underlying system's dynamics are highly likely to result in instability, even for a nominally stable controller. As shown in Fig. 8, the optimal experimental design results in lower structured singular values, for both of the two flame locations considered in this work, at all frequencies. This shows the degree to which optimal experimental design can furnish stronger robustness guarantees compared to the benchmark experiment. This improvement in robustness guarantees is particularly important for the second case (i.e., the second flame location), where the structured singular value exceeds 1.0 neat 480Hz, indicating very poor robustness. The use of optimal experimental design mitigates this issue, achieving a much stronger robustness guarantee.

Conclusions

In this paper, we consider a thermoacoustic model identification and build an experiment to validate the hypothesis of improving model identification accuracy with applications of optimal experimental designs. We start from the derivation of a thermoacoustic model including a linear time-lag model that describes the heat release dynamics in a premixed flame in a Rijke tube.

As a benchmark case, we apply a linear chirp signal with slowly varying frequencies as the input to achieve the frequency response of the system. Using the least mean square method, we estimate parameters $\hat{\tau}$ and $\hat{\beta}$ from experiments by minimizing the RMS of the magnitude error between measured and estimated transfer functions. It turns out that it is difficult to achieve an accurate structured model identification with the

chirp signal because the estimated thermoacoustic model fails to describe the system dynamics accurately at every single frequency within the interested frequency range.

For a comparison to the benchmark case, we apply Fisher identifiability analysis to optimize the experimental designs for parameter estimates accuracy improvement. Optimal experimental design outputs two frequencies and one sensor placement for model identification. We use the same method as that for the benchmark case to estimate the time lag τ and amplification factor β with uncertainties quantified. The optimal experiment indeed achieves more accurate parameter estimates with smaller uncertainties. Additionally, it saves 75% of time in model identification experiments and 90% of the computational time in estimating parameters as compared to the benchmark case.

A negative correlation exists between the system's model uncertainties and the robustness of the optimal LQG controller, which is within expectation. The system identification with optimal uncertainty can lead to a controller design with more confidence in terms of the robustness.

The spirit of this article is to show, using a laboratory experiment, the degree to which optimal experimental design can lead to more accurate combustion instability models, and therefore stronger robustness guarantees for active combustion stability controllers. To the best of the authors' knowledge, this article is the first contribution to the literature that uses laboratory experiments to illustrate these important insights. By necessity, we perform this illustration for a specific combustion stability model (namely, the so-called "n-tau" model), a specific stability controller (namely, LQG control), and a specific combustor (namely, a flame-driven Rijke tube). However, the primary tool illustrated in the paper (namely, Fisher information-based optimal experimental design) is applicable to other combustion stability control problems, and has been widely adopted

in the literature for experimental design problems beyond the field of combustion stability control.

Acknowledgment

Reference

Annaswamy, A. M. *et al.* (2000) 'Thermoacoustic instability: Model-based optimal control designs and experimental validation', *IEEE Transactions on control systems technology*. IEEE, 8(6), pp. 905–918.

Avdonin, A. *et al.* (2018) 'Uncertainty quantification and sensitivity analysis of thermoacoustic stability with non-intrusive polynomial chaos expansion', *Combustion and Flame*. Elsevier, 189, pp. 300–310.

Balasubramanian, K. and Sujith, R. I. (2008) 'Thermoacoustic instability in a Rijke tube: Non-normality and nonlinearity', *Physics of Fluids*. AIP, 20(4), p. 44103.

Bauerheim, M. *et al.* (2014) 'Uncertainty quantification of thermo-acoustic instabilities in annular combustors', in *Proceedings of the Summer Program*, pp. 209–218.

Bernier, D. *et al.* (2003) 'Transfer function measurements in a model combustor : Application to adaptive instability control', *Combustion Science and Technology*, 2202.

Bittanti, S. *et al.* (2002) 'Identification of a model for thermoacoustic instabilities in a Rijke tube', *IEEE Transactions on control systems technology*. IEEE, 10(4), pp. 490–502.

Bodén, H. and Åbom, M. (1986) 'Influence of errors on the two-microphone method for measuring acoustic properties in ducts', *The Journal of the Acoustical Society of America*, 79(2), pp. 541–549. doi: 10.1121/1.393542.

Celik, M. *et al.* (1995) 'Pole-zero computation in microwave circuits using multipoint Padé approximation', *IEEE Transactions on Circuits and Systems I: Fundamental Theory and Applications*. IEEE, 42(1), pp. 6–13.

Chen, X. *et al.* (2019) 'Optimizing the design of a Rijke tube experiment for combustion stability model identifiability', *American Control Conference (submitted)*.

Crocco, L. and Cheng, S.-I. (1956) 'Theory of combustion instability in liquid propellant rocket motors', *Butterworths Scientific Publications*, 21, pp. 163–178.

Dines, P. J. (1984) *Active Control of Flame Noise*. University of Cambridge.

Dowling, A. P. and Morgans, A. S. (2005) 'Feedback control of combustion oscillations', *Annu. Rev. Fluid Mech.* Annual Reviews, 37, pp. 151–182.

Dowling, A. P. and Stow, S. R. (2003) 'Acoustic Analysis of Gas Turbine Combustors', *Journal of Propulsion and Power*. American Institute of Aeronautics and Astronautics, 19(5), pp. 751–764. doi: 10.2514/2.6192.

Dupere, I. D. J. and Dowling, A. P. (2005) 'The use of Helmholtz resonators in a practical combustor', *Journal of engineering for gas turbines and power*. American Society of Mechanical Engineers Digital Collection, 127(2), pp. 268–275.

Epperlein, J. P., Bamieh, B. and Åström, K. J. (2015) 'Thermoacoustics and the Rijke Tube-Experiments, Identification and Modeling', (March), pp. 57–77.

Forman, J. C. *et al.* (2012) 'Genetic identification and fisher identifiability analysis of the Doyle--Fuller--Newman model from experimental cycling of a LiFePO4 cell', *Journal of Power Sources*. Elsevier, 210, pp. 263–275.

Freitag, E. *et al.* (2006) 'Pressure influence on the flame transfer function of a premixed swirling flame', in *Turbo Expo: Power for Land, Sea, and Air*, pp. 477–486.

Gelbert, G. *et al.* (2012) 'Feedback control of unstable thermoacoustic modes in an annular Rijke tube', *Control Engineering Practice*. Elsevier, 20(8), pp. 770–782.

Hathout, J. P. *et al.* (1998) 'A model-based active control design for thermoacoustic instability', *Combustion science and technology*. Taylor & Francis, 132(1–6), pp. 99–138.

Heckl, M. A. (1988) 'Active control of the noise from a rijke tube', *Journal of Sound and Vibration*. Academic Press Limited, 124(1), pp. 117–133. doi: 10.1016/S0022-460X(88)81408-1.

Heckl, M. A. (2010) 'the rijke tube: A green's function approach in the frequency domain', *Acta Acustica united with Acustica*. S. Hirzel Verlag, 96(4), pp. 743–752.

Kim, D. *et al.* (2010) 'Effect of Flame Structure on the Flame Transfer Function in a Premixed Gas Turbine Combustor', *Journal of Engineering for Gas Turbines and Power*, 132(2), p. 021502. doi: 10.1115/1.3124664.

Koshigoe, S., Komatsuzaki, T. and Yang, V. (1999) 'Adaptive Control of Combustion Instability with On-Line System Identification', *Journal of Propulsion and Power*, 15(3), pp. 383–389.

Lang, W., Poinsot, T. and Candel, S. (1987) 'Active control of combustion instability', *Combustion and Flame*. Elsevier, 70(3), pp. 281–289.

Lieuwen, T. *et al.* (1999) 'A Mechanism of Combustion Instability in Lean Premixed Gas Turbine Combustors', *Journal of Engineering for Gas Turbines and Power*, 123(1), p. 182. doi: 10.1115/1.1339002.

Lieuwen, T. C. *et al.* (2001) 'A Mechanism of Combustion Instability in Lean Premixed Gas Turbine Combustors', *Journal of Engineering for Gas Turbines and Power*, 123(1), pp. 182–189. doi: 10.1115/1.1339002.

Lieuwen, T. C. and Yang, V. (2005) *Combustion instabilities in gas turbine engines: operational experience, fundamental mechanisms, and modeling*. American Institute of Aeronautics and Astronautics.

Magri, L. *et al.* (2016) 'Stability analysis of thermo-acoustic nonlinear eigenproblems in annular combustors. Part II. Uncertainty quantification', *Journal of Computational Physics*. Elsevier Inc., 325, pp. 411–421. doi: 10.1016/j.jcp.2016.08.043.

Manchester, I. R. (2010) 'Input design for system identification via convex relaxation', in *49th IEEE Conference on Decision and Control (CDC)*, pp. 2041–2046.

Mehra, R. (1974) 'Optimal input signals for parameter estimation in dynamic systems - Survey and new results', *IEEE Transactions on Automatic Control*, 19(6), pp. 753–768. doi: 10.1109/TAC.1974.1100701.

Mendoza, S. *et al.* (2016) 'Optimization and experimental validation of a thermal cycle that maximizes entropy coefficient fisher identifiability for lithium iron phosphate cells', *Journal of Power Sources*. Elsevier, 308, pp. 18–28.

Mensah, G. A., Magri, L. and Moeck, J. P. (2018) 'Methods for the calculation of thermoacoustic stability boundaries and monte carlo-free uncertainty quantification', *Journal of Engineering for Gas Turbines and Power*. American Society of Mechanical

Engineers, 140(6), p. 61501.

Morgans, A. and Dowling, A. (2005) 'Model-Based Control of a Rijke Tube Combustion Instability', *11th AIAA/CEAS Aeroacoustics Conference*, (May), pp. 23–25. doi: 10.2514/6.2005-2909.

Murray, R. M. *et al.* (1998) 'System identification for limit cycling systems: a case study for combustion instabilities', in *Proceedings of the 1998 American Control Conference. ACC (IEEE Cat. No. 98CH36207)*, pp. 2004–2008.

Murugappan, S *et al.* (2003) 'Optimal control of a swirl-stabilized spray combustor using system identification approach', *Combustion Science and Technology*, 2202. doi: 10.1080/00102200302360.

Murugappan, S. *et al.* (2003) 'Optimal control of a swirl-stabilized spray combustor using system identification approach', *Combustion Science and Technology*, 175(1), pp. 55–81. doi: 10.1080/00102200302360.

Nair, V., Sarkar, S. and Sujith, R. I. (2013) 'Uncertainty quantification of subcritical bifurcations', *Probabilistic Engineering Mechanics*. Elsevier, 34, pp. 177–188.

Ndiaye, A. *et al.* (2015) 'Uncertainty quantification of thermoacoustic instabilities in a swirled stabilized combustor', in *ASME Turbo Expo 2015: Turbine Technical Conference and Exposition*, p. V02CT45A023--V02CT45A023.

Palies, P. *et al.* (2010) 'The combined dynamics of swirler and turbulent premixed swirling flames', *Combustion and Flame*. The Combustion Institute., 157(9), pp. 1698–1717. doi: 10.1016/j.combustflame.2010.02.011.

Palies, P. *et al.* (2011) 'Modeling of premixed swirling flames transfer functions', *Proceedings of the Combustion Institute*. Elsevier Inc., 33(2), pp. 2967–2974. doi: 10.1016/j.proci.2010.06.059.

Pronzato, L. (2008) 'Optimal experimental design and some related control problems', *Automatica*. Elsevier, 44(2), pp. 303–325.

Rigas, G. *et al.* (2016) 'Experimental sensitivity analysis and control of thermoacoustic systems', *Journal of Fluid Mechanics*, 787, pp. 1–11.

Samarasinghe, J. *et al.* (2017) 'The Effect of Fuel Staging on the Structure and Instability Characteristics of Swirl-Stabilized Flames in a Lean Premixed Multinozzle

Can Combustor', *Journal of Engineering for Gas Turbines and Power*. ASME, 139(12), pp. 121504–121510.

Schuller, T., Durox, D. and Candel, S. (2003) 'A unified model for the prediction of laminar flame transfer functions: comparisons between conical and V-flame dynamics', *Combustion and Flame*. Elsevier, 134(1–2), pp. 21–34.

Selimefendigil, F., Sujith, R. I. and Polifke, W. (2011) 'Identification of heat transfer dynamics for non-modal analysis of thermoacoustic stability', *Applied Mathematics and Computation*. Elsevier Inc., 217(11), pp. 5134–5150.

Seume, J. R. *et al.* (1997) 'Application of active combustion instability control to a heavy duty gas turbine', in *ASME 1997 Turbo Asia Conference*, p. V001T05A007--V001T05A007.

Sharma, A. and Fathy, H. K. (2014) 'Fisher identifiability analysis for a periodically-excited equivalent-circuit lithium-ion battery model', in *2014 American Control Conference*, pp. 274–280.

Silva, C. F. *et al.* (2017) 'Uncertainty Quantification of Growth Rates of Thermoacoustic Instability by an Adjoint Helmholtz Solver', *Journal of Engineering for Gas Turbines and Power*, 139(1), p. 011901. doi: 10.1115/1.4034203.

Steele, R. C. *et al.* (2000) 'Passive control of combustion instability in lean premixed combustors', *Journal of Engineering for Gas Turbines and Power*. American Society of Mechanical Engineers Digital Collection, 122(3), pp. 412–419.

Subramanian, P., Sujith, R. I. and Wahi, P. (2013) 'Subcritical bifurcation and bistability in thermoacoustic systems', *Journal of Fluid Mechanics*, 715, pp. 210–238.

Vaudrey, M. A. (2001) *Adaptive Control Methods for Non-Linear Self-Excited Systems*. Virginia Polytechnic Institute and State University.

Venkataraman, K. K. *et al.* (1999) 'Mechanism of Combustion Instability in a Lean Premixed Dump Combustor', *Journal of Propulsion and Power*, 15(6), pp. 909–918. doi: 10.2514/2.5515.